

# Electronic Supplementary Information for: Photoredox capacity expanded by the Cu site of CuFe-Mabiq

Matthias Huber,<sup>a,b</sup> Ajeet Kumar,<sup>b</sup> Jürgen Hauer,<sup>b</sup> Erling Thyryhaug,<sup>\*,b</sup> and Corinna R. Hess<sup>\*a,b</sup>

<sup>a</sup> Faculty of Chemistry and Pharmacy, University of Regensburg, 93053 Regensburg, Germany.

<sup>b</sup> TUM School of Natural Sciences and Catalysis Research Center, Technical University of Munich, 85748 Garching, Germany.

Email: [corinna.hess@ur.de](mailto:corinna.hess@ur.de); [erling.thyryhaug@tum.de](mailto:erling.thyryhaug@tum.de)

## Table of Contents

1	General.....	3
2	Instrumentation.....	3
3	Synthesis.....	6
4	Crystallography.....	7
5	UV/Vis Spectra of the Fe- and Cu/Fe-Mabiq complexes.....	11
6	Ultrafast Transient Spectroscopy.....	12
7	UV/Vis Spectra during photoreduction.....	15
8	Comparison of spectra: Photoreduction vs Electrolysis.....	23
9	Photoreduction analysis.....	29
10	Fe <sup>III</sup> (Mabiq)Cl <sub>2</sub> Photochemistry.....	31

## 1 General

All chemicals were purchased from Sigma Aldrich and used without further purification unless noted otherwise. Metal compounds were synthesized in an inert atmosphere glove box (Ar), using anhydrous solvents. Dry solvents were obtained from an MBraun SPS, deoxygenated via freeze-pump-thaw cycles and stored over 3 Å (MeCN, pentane) or 4 Å activated molecular sieves. Solvents for electrochemical and photochemical reactions were filtered over activated aluminum oxide prior to use (activated, standard grade, neutral, Brokmann I, 58 Å pore size). Tetrabutylammonium hexafluorophosphate ( $[\text{N}(n\text{-Bu})_4]\text{PF}_6$ ) was recrystallized three times from ethanol,<sup>1</sup> and ferrocene was sublimed prior to use. HMabiq,<sup>2</sup>  $[\text{Fe}(\text{Mabiq})]$  (**1<sup>red</sup>**),  $[\text{Fe}(\text{Mabiq})\text{Cl}_2]$ ,<sup>3</sup>  $[\text{Fe}(\text{Mabiq})(\text{MeCN})_2]\text{OTf}$  (**1**),  $[\text{Cu}(\text{Xantphos})\text{Fe}(\text{Mabiq})(\text{MeCN})(\text{OTf})]\text{OTf}$  (**2**),  $[\text{Cu}(\text{Xantphos})(\text{OTf})]$ ,<sup>4</sup> 9,9-dimethyl-9*H*-xanthene-4,5-diyl)bis(bis(4-methoxyphenyl)phosphane (Xantphos<sup>OMe</sup>)<sup>5</sup> and 1,3-dimethyl-2-phenyl-2,3-dihydro-1*H*-benzo[*d*]imidazole (BIH)<sup>6</sup> were synthesized as previously described. We note that after crystallization, **2** is obtained either with one MeCN and one OTf ligand or two OTf ligands bound to the Fe-centre. Fig. 1 in the manuscript depicts the former structure.

## 2 Instrumentation

Electronic spectra were measured on an Agilent Cary 60 UV-Vis spectrophotometer.

Microanalysis were carried out by the analytical department of the University of Regensburg using a Vario micro cube.

Electrochemical measurements (Cyclic Voltammetry, Controlled Potential Electrolysis) were carried out with a BioLogic SP200 potentiostat with EC-Lab software, using a glassy carbon plate (35 mm x 10 mm x 3 mm, HTW Germany) as working electrode and a Pt mesh as counter electrode. Prior to use, the glassy carbon plate was polished with 0.05 μm alumina suspensions (CH Instruments Inc., USA). Ag/AgNO<sub>3</sub> (10 mM AgNO<sub>3</sub> and 0.1 M  $[\text{N}(n\text{-Bu})_4]\text{PF}_6$  in MeCN) was used as the reference electrode,

separated via a Vycor 3535 frit (Advanced Glass & Ceramics, Holden, MA). A custom-made H-cell adapted from Elgrishi et al.,<sup>7</sup> where the working and counter compartment are separated from each other via a fine porous glass frit (POR 4) was used. Either 6 mL (1) or 4 mL (2) of a 500  $\mu$ M solution of the respective complex and 0.1 M  $[\text{N}(n\text{-Bu})_4]\text{PF}_6$  in dry, deoxygenated MeCN were added to the working compartment, and 3 mL of electrolyte solution (0.1 M  $[\text{N}(n\text{-Bu})_4]\text{PF}_6$  in dry, deoxygenated MeCN) were added to the counter compartment of the cell in an Ar filled glovebox. For CV measurements, a scan rate of 100 mV/s was applied. Potentials are reported with reference to an internal standard of ferrocenium/ferrocene ( $\text{Fc}^{+/0}$ , given by  $V_{\text{Fc}}$ ).

For the photoreduction of our complexes, the quantum yield (QY) of the reaction was determined using a quantum yield determination setup (QYDS) as described earlier.<sup>8,9</sup> The components are contained within a black box to protect the sample from any external light sources, and the experimenter from the intense stray light. A high-power LED ( $\lambda_{\text{exc}} = 455 \text{ nm}$ ) of type LD-CQ7P-1U3U produced by Osram was used as the excitation light source. The current for the LED was controlled by a power supply of type RND 320-KA3005P from RND lab. The lens system consists of a Thorlabs aspheric condenser lens ( $f = 32 \text{ mm}$ , 50 mm diameter) and a Thorlabs plano-convex lens ( $f = 100 \text{ mm}$ , 50 mm diameter). The light bundle was imaged through an aperture (8 mm x 8 mm square) in front of the cuvette holder and onto the middle of the cuvette. A shutter was placed between the lens system and the aperture to interrupt the incoming light beam during the measurement, as warranted. The 10 mm x 10 mm fused silica sample cuvette was fitted with a ground glass joint. The volume of the sample solutions was 2 mL. During the irradiation period the solutions were rigorously stirred. The transmitted light power of the sample solution ( $P_{\text{sample}}$ ) was detected using a Thorlabs power meter of type S175C. To determine the reference power ( $P_{\text{ref}}$ ) a cuvette containing 2 mL of solvent was irradiated using the same input power settings as for the sample. All experiments were performed at  $P_{\text{ref}} = 668 \pm 12 \text{ mW}$ . The measurements were monitored and data was recorded using a Labview program developed by the Riedle group, which displays the total illumination time. The incoming light beam was interrupted *via*

a shutter control box, at which point the timer also was paused. The cuvette was subsequently transferred to the Cary 60 UV/Vis instrument and an absorption spectrum was recorded. The cuvette was placed back into the QYDS and the illumination was continued. For each time period the illumination time ( $\Delta t$ ), transmitted power ( $P_{\text{sample}}$ ) and the LED driver voltage ( $U$ ) and current ( $I$ ) were recorded in a log file.

The quantum yield was calculated as previously reported<sup>4</sup> from the amount of product formed divided by the number of absorbed photons.<sup>8, 10, 11</sup> The number of absorbed photons was calculated from the difference of the reference power and the power reaching the photometer.<sup>8</sup> To determine the amount of product formed, the absorption at two different wavelengths was monitored. In the photo-reduction of both **1** and **2**, we found that each successive reduction step was essentially complete before further reduction took place. As such, during each reduction step (*e.g.* **1** to **1<sup>red</sup>**) only two species were present in solution at significant concentration. Thus, we could determine the yield of a given reduction step directly from the overall reduction kinetics simply by modeling the data in time-intervals where only the relevant species were present. While this simplified procedure is not generally applicable for multi-step reactions, it was here facilitated by our knowledge of the molecular absorption coefficients of the involved species (allowing determination of the concentrations of the species of interest) and that only two species were present in meaningful concentrations in any given time-interval. Consequently, the quantum yields could be determined for each individual reaction using standard procedures for simple reactions of type  $\{A + B \rightarrow P\}$ .

The samples were prepared under an argon atmosphere inside a glove box and under red light conditions. A cuvette fitted with a ground glass joint and stir bar was used for all measurements. The sealed cuvette was removed from the glove box, ensuring that no light reached the sample, and an absorption spectrum was taken. This measurement gave the reference absorption spectrum prior to LED illumination ( $t = 0$  spectrum). The cuvette was then transferred into the QYDS setup, the sample

was irradiated for various time periods and an absorption spectrum was measured after each time period.

Photoreduction experiments with BIH: 44.9 mg (2000 equiv.), 22.4 mg (1000 equiv.) or 11.2 mg (500 equiv) of BIH were dissolved in 1.9 mL of MeCN. 100  $\mu$ L of a 1 mM stock solution of the complex in the same solvent were added. [complex] = 50  $\mu$ M, [BIH] = 100 mM, 50 mM or 25 mM.

Photoreduction experiments with TEA: 100  $\mu$ L of a 1 mM stock solution of the complex in MeCN were added to 1.872 mL of MeCN and 27.9  $\mu$ L of Et<sub>3</sub>N. [complex] = 50  $\mu$ M, [Et<sub>3</sub>N] = 100 mM.

Photoreduction of Fe(Mabiq)Cl<sub>2</sub>: 100  $\mu$ L of a 1 mM stock solution of Fe(Mabiq)Cl<sub>2</sub> in DCM were diluted with 0.9 mL DCM and 1.0 mL MeCN. [Fe(Mabiq)Cl<sub>2</sub>] = 50  $\mu$ M.

### 3 Synthesis

**[Cu(Xantphos)Fe(Mabiq)(OTf)] (2<sup>red</sup>):** A solution of 21.6 mg (27.3  $\mu$ mol, 1.00 equiv) of [Cu(Xantphos)OTf] in THF was added to a solution of 16.3 mg (27.3  $\mu$ mol, 1.00 equiv) of **1<sup>red</sup>** in THF, resulting in an immediate color change from blue to green. After stirring at room temperature for 30 min, the solution was filtered over Celite, concentrated under vacuum, and recrystallized by slow diffusion of pentane into the solution yielding **2<sup>red</sup>** (27.8 mg, 73.3%).

Elemental analysis calc. (%) for C<sub>73</sub>H<sub>65</sub>CuF<sub>3</sub>FeN<sub>8</sub>O<sub>4</sub>P<sub>2</sub>S: C, 63.14, H, 4.72, N, 8.07, S, 2.31; found C, 62.64, H, 5.01, N, 7.97, S, 2.12. UV-Vis [ $\lambda_{\max}$ , nm ( $\epsilon$ , 10<sup>3</sup> M<sup>-1</sup>cm<sup>-1</sup>), in MeCN]: 353 (28.1), 460 (sh), 637 (12.6).

**[Cu(Xantphos<sup>OMe</sup>)Fe(Mabiq)(OTf)] (2<sup>red,OMe</sup>)** was synthesized as per the protocol described for **2<sup>red</sup>** but using Xantphos<sup>OMe</sup> to generate [Cu(Xantphos<sup>OMe</sup>)(OTf)]. Single crystals suitable for X-Ray diffractometry were obtained by slow diffusion of pentane into a solution of **2<sup>red,OMe</sup>** in THF.

## 4 Crystallography

Crystallographic data were collected on a Rigaku XtaLAB Synergy DW (HyPix-Arc 150) diffractometer with Cu-K $\alpha$  radiation ( $\lambda = 1.54184 \text{ \AA}$ ). The measurements were performed on single crystals overlaid with perfluorinated ether. A suitable crystal was transferred to the diffractometer on top of a micro mount loop. The measurements were carried out at 123 K using a nitrogen stream. Semi-empirical multi-scan absorption corrections<sup>12, 13</sup> were applied on the data using the program CrysAlisPro (Rigaku Oxford Diffraction, 2021). Structures were solved by SHELXT<sup>14</sup> with the aid of successive difference Fourier maps and were refined against all data using SHELXL<sup>15</sup> in conjunction with Olex2 as the graphical interface.<sup>16</sup> Full-matrix least squares refinements were carried out by minimizing on F<sup>2</sup>.<sup>17</sup> Hydrogen atoms were assigned to ideal positions and refined isotropically using a riding model.

Disordered solvent molecules were treated as a diffuse contribution to the overall scattering without specific atom positions using a solvent mask. Overall, 248 electrons corresponding to 3 residual THF molecules were determined. Images of the crystal structures were generated using Mercury.<sup>18</sup> CCDC 2391634 contains the supplementary crystallographic data for this paper.

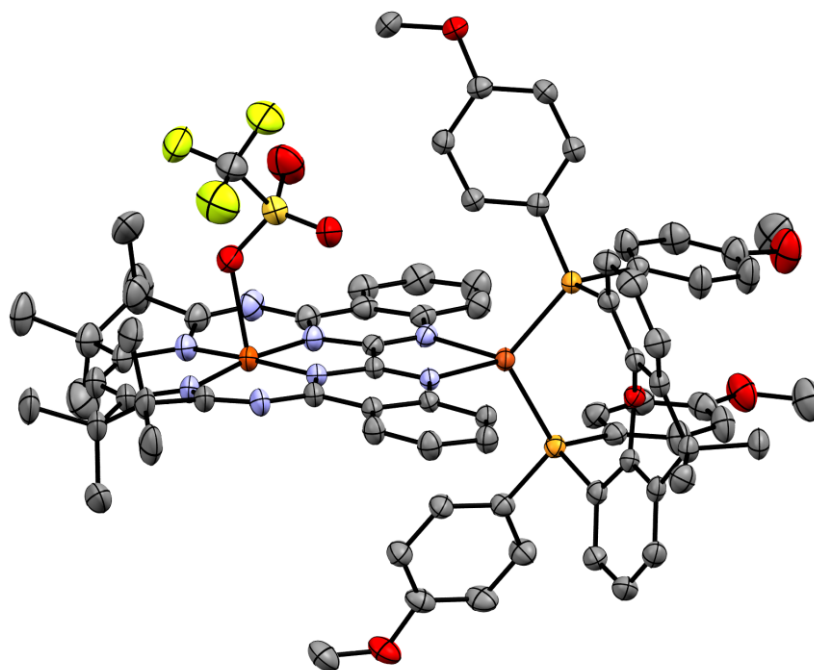


Figure S1: ORTEP style representation of of  $2^{\text{red,OMe}}$  in the solid state. Ellipsoids are shown at 50% probability level and hydrogen atoms are omitted for clarity.

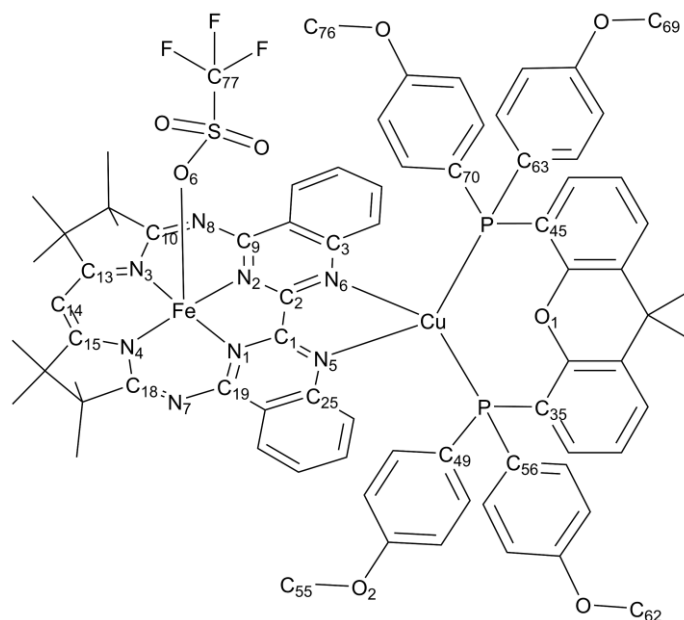


Chart S1: Atomic numbering scheme for  $2^{\text{red,OMe}}$ .

Table S1: Crystallographic refinement data for **2<sup>red,OMe</sup>**.

---

Empirical formula	C <sub>77</sub> H <sub>73</sub> CuF <sub>3</sub> FeN <sub>8</sub> O <sub>8</sub> P <sub>2</sub> S
Formula weight	1508.82
Crystal system	triclinic
Space group	P $\bar{1}$
a (Å)	11.2420(2)
b (Å)	18.8746(3)
c (Å)	20.4850(2)
$\alpha$ (°)	89.5000(10)
$\beta$ (°)	76.0950(10)
$\gamma$ (°)	81.2580(10)
Volume (Å <sup>3</sup> )	4168.53(11)
Z	2
Density (calculated) (g/cm <sup>3</sup> )	1.202
Absorption coefficient (mm <sup>-1</sup> )	2.806
F(000)	1566
Reflections collected	280021
Independent reflections/R(int)	16934/0.0428
Data / restraints / parameters	16934 / 0 / 925
Goodness-of-fit on F <sup>2</sup>	1.082
$\Delta/\sigma_{\max}$	0.002
CCDC number	2391634

---

Table S2: Select bond distances for **2<sup>red,OMe</sup>** following the numbering scheme indicated in Chart S1.

Cu1-P1	2.2872(5)	Cu1-P2	2.2745(5)
Cu1-N5	2.1263(16)	Cu1-N6	2.1100(16)
Fe1-O6	2.2451(17)	Fe1-N1	1.9141(17)
Fe1-N2	1.9079(18)	Fe1-N3	1.9036(19)
Fe1-N4	1.9063(19)	P1-C35	1.838(2)
P1-C49	1.819(2)	P1-C56	1.830(2)
P2-C45	1.830(2)	P2-C63	1.827(2)
P2-C70	1.816(2)	N1-C1	1.362(2)
N1-C19	1.361(3)	N2-C2	1.368(2)
N2-C9	1.366(3)	N3-C10	1.358(3)
N3-C13	1.369(3)	N4-C15	1.371(3)
N4-C18	1.365(3)	N5-C1	1.310(2)
N5-C25	1.386(2)	N6-C2	1.295(3)
N6-C3	1.394(3)	N7-C18	1.318(3)
N7-C19	1.341(3)	N8-C9	1.345(3)
N8-C10	1.317(3)	C1-C2	1.472(3)
C13-C14	1.377(4)	C14-C15	1.388(4)

Table S3: Select bond angles for **2<sup>red,OMe</sup>** following the numbering scheme indicated in Chart S1.

P2-Cu1-P1	113.63(2)	N5-Cu1-P1	114.23(5)
N5-Cu1-P2	115.14(5)	N6-Cu1-P1	111.51(5)
N6-Cu1-P2	119.31(5)	N6-Cu1-N5	78.62(6)
N1-Fe1-O6	98.23(7)	N2-Fe1-O6	94.66(7)
N2-Fe1-N1	84.56(7)	N3-Fe1-O6	86.73(7)
N3-Fe1-N1	173.66(8)	N3-Fe1-N2	91.12(8)
N3-Fe1-N4	93.12(8)	N4-Fe1-O6	91.81(8)
N4-Fe1-N1	90.69(8)	N4-Fe1-N2	172.46(8)
C19-N1-C1	117.68(16)	C9-N2-C2	117.25(18)
N5-C1-C2	117.49(17)	N6-C2-C1	117.93(17)
C13-C14-C15	126.3(2)		

## 5 UV/Vis Spectra of the Fe- and Cu/Fe-Mabiq complexes

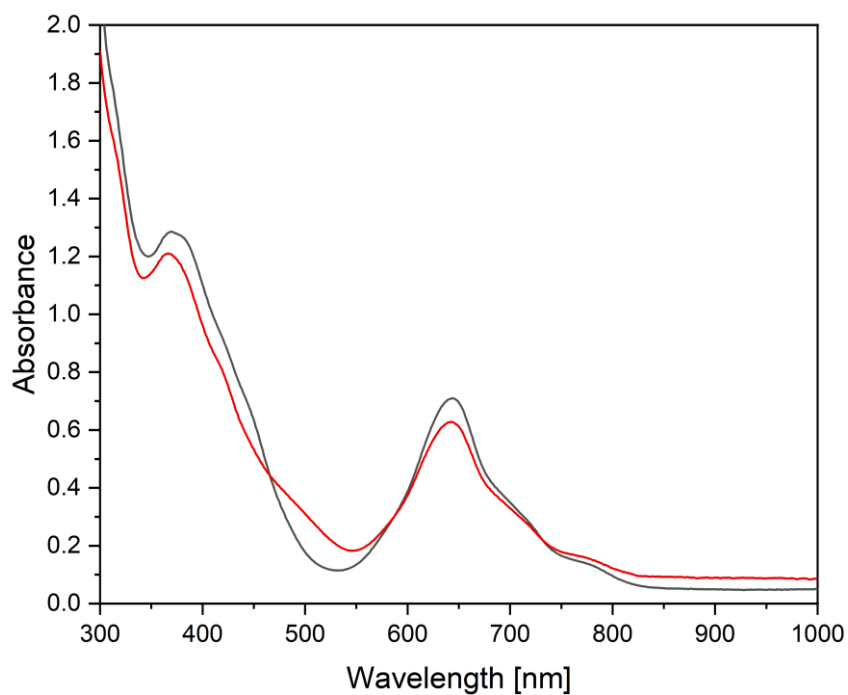


Figure S2: UV/Vis absorption spectra of  $2^{\text{red}}$  (black) and  $2^{\text{red,OMe}}$  (red) in THF.

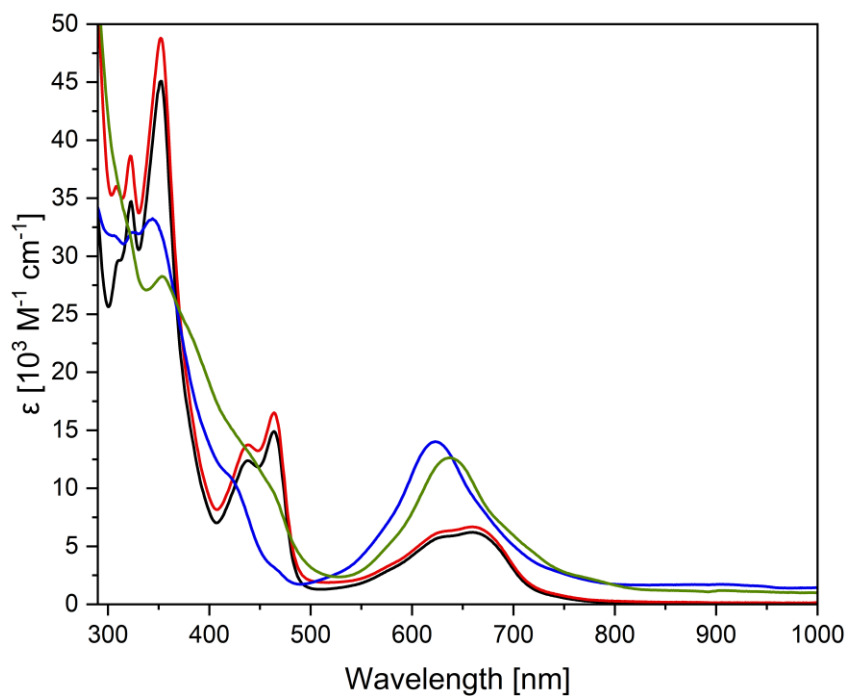


Figure S3: UV/Vis absorption spectra of **1** (black), **2** (red),  $1^{\text{red}}$  (blue) and  $2^{\text{red}}$  (green) in MeCN.

## 6 Ultrafast Transient Spectroscopy

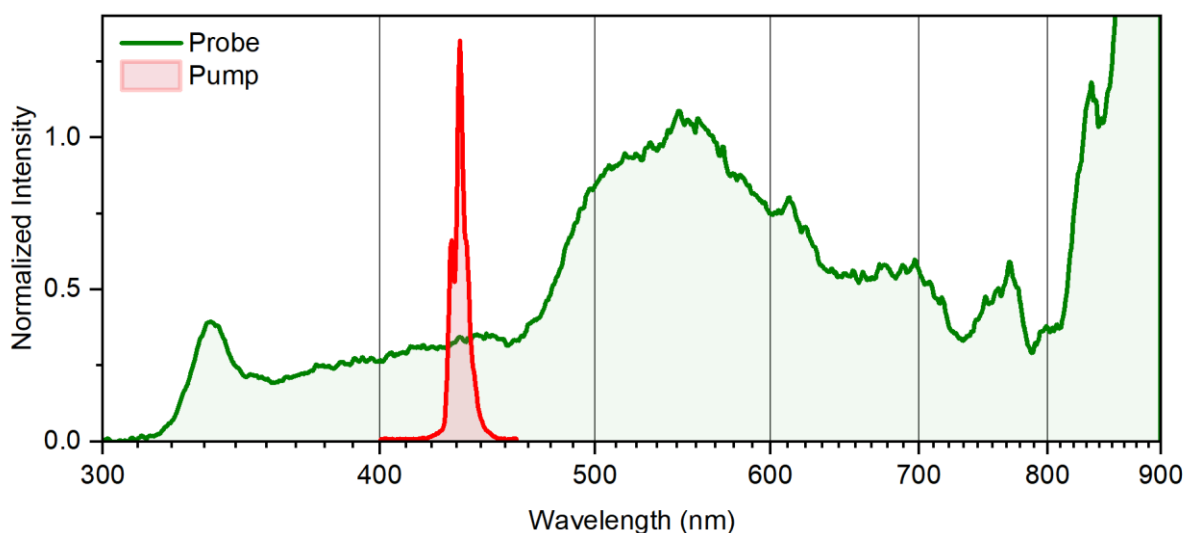


Figure S4: Spectra of pump (red) and probe (green) pulses in the ultrafast TA experiment. The probe was generated using the NIR seed output from a HCF. Note that the X-axis is plotted on reciprocal scale.

For TA measurements we used a home-built TA setup based on hollow core fiber (HCF) supercontinuum.<sup>19</sup> A commercial Ti:Sa laser amplifier (Coherent Legend ElitecDuo), delivering 25 fs laser pulses at 800 nm central wavelength with 2.4 mJ per pulse at 5 kHz repetition rate, was used as a fundamental light source. Pulse energies were attenuated to 240  $\mu$ J by a combination of  $\lambda/2$  plate and a thin film polarizer. The transmitted p-polarized light through the polarizer was focused into an Argon-filled 1m long capillary fiber (Ultrafast Innovations) to achieve spectral broadening. The efficiency of the HCF output was measured to more than 60%.<sup>19</sup> The collimated HCF spectrum was passed through a chirped mirror compressor (Ultrafast Innovations) with mirror reflective in the 500-1000 nm spectral range. After the compressor, the light passed through a beam splitter which reflects lights between 450-900 nm and transmits near infrared wavelength ( $>900$  nm). The transmitted NIR lights was used to seed a 5 mm thick CaF<sub>2</sub> crystal to generate broadband super-continuum for probe pulses (Figure S4). After super-continuum generation, aluminum mirrors were used to steer the beam to the sample position.

The reflected visible lights from the beam splitter was passed through a 4-f grating compressor in order to filter the spectrum between 840-900 nm. This spectrum was frequency doubled using a 300  $\mu\text{m}$  thick BBO crystal, resulting in pump pulses centered at 435 nm. Using a broadband half-wave plate, the polarization of the pump pulse was set to magic angle ( $54.7^\circ$ ) with respect to the probe pulse.

Both pump and probe pulses were focused at the sample position using a 250 mm focal length spherical mirror. The  $1/e^2$  beam waist of the focused pump and probe beam at the sample position were close to 190 and 92  $\mu\text{m}$  respectively, as determined by a beam profiler (CMOS-1201, Cinogy). After the sample, the transmitted probe pulses were detected on a grating spectrometer-equipped sCMOS camera (ANDOR Kymera 328i).

All experiments were performed in custom made air tight 1 mm pathlength quartz cells equipped with a Schlenk line connector. For the measurements shown in the manuscript, the excitation energy was 30 nJ per pulse. The probe pulse energy was kept at less than  $1/80^{\text{th}}$  of the pump pulse energy. The cuvette was continuously moved perpendicularly to the laser beam path during the measurements in order to avoid photo-damage or photo-bleaching of the sample. The time resolution of the experiment was estimated to approximately 65 fs by fitting the width of coherent artifact at 500 nm.

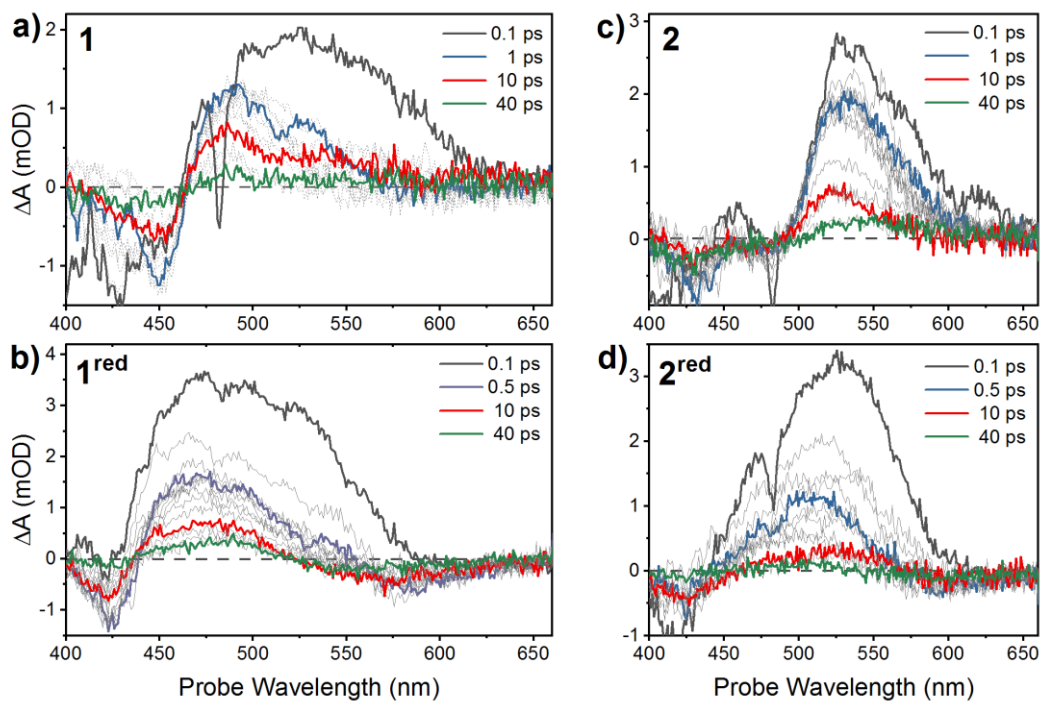


Figure S5: Transient absorption spectra at selected pump-probe delays, extracted from the full two-dimensional dataset shown in manuscript Figure 1.

## 7 UV/Vis Spectra during photoreduction

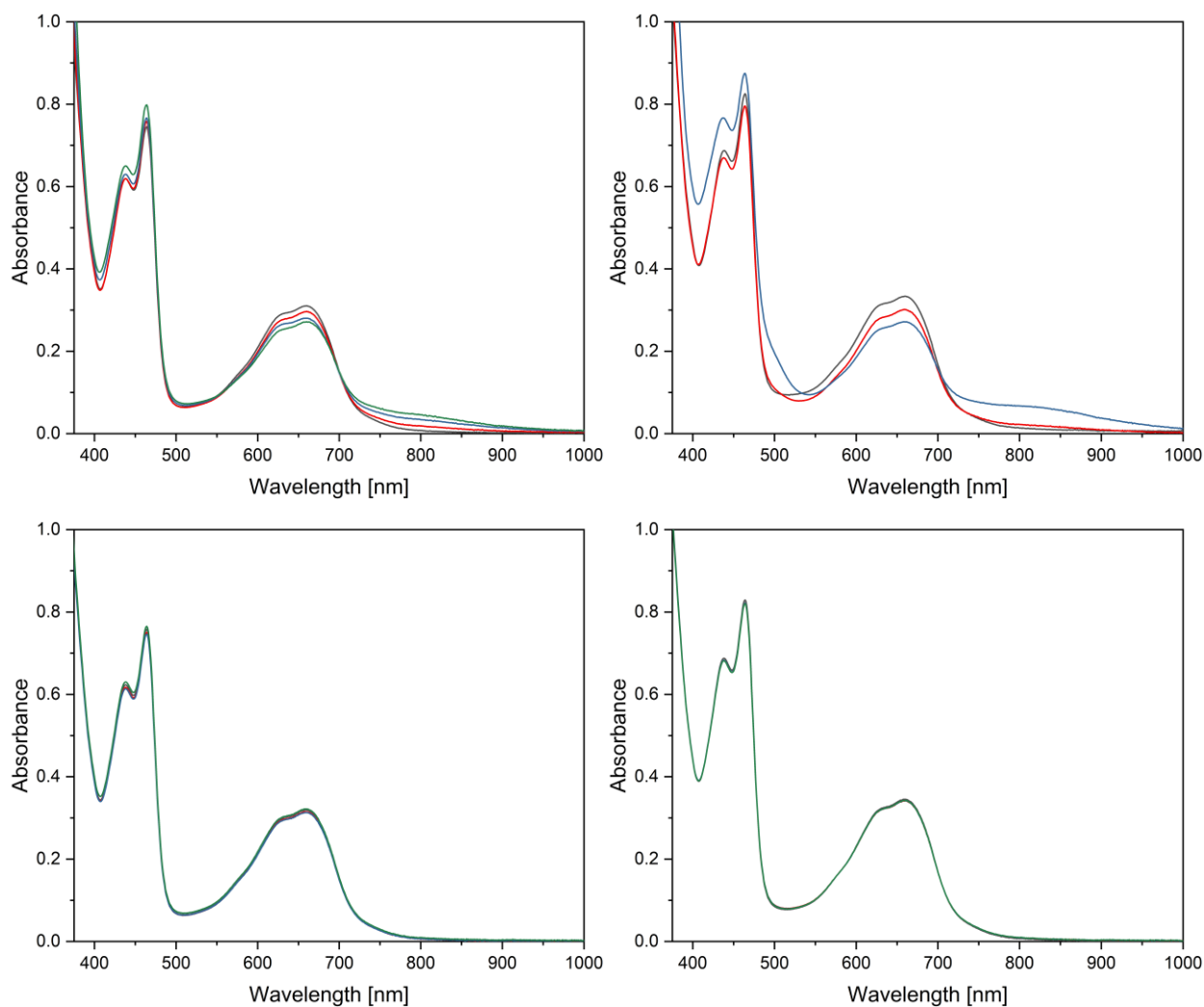


Figure S6: UV/Vis absorption spectra of 50  $\mu\text{M}$  **1** (left panels) and **2** (right panels) in the absence (black) and presence of 25 mM (red), 50 mM (blue) and 100 mM (green) SED; all in MeCN. Top: SED = BIH, bottom: SED =  $\text{Et}_3\text{N}$ .

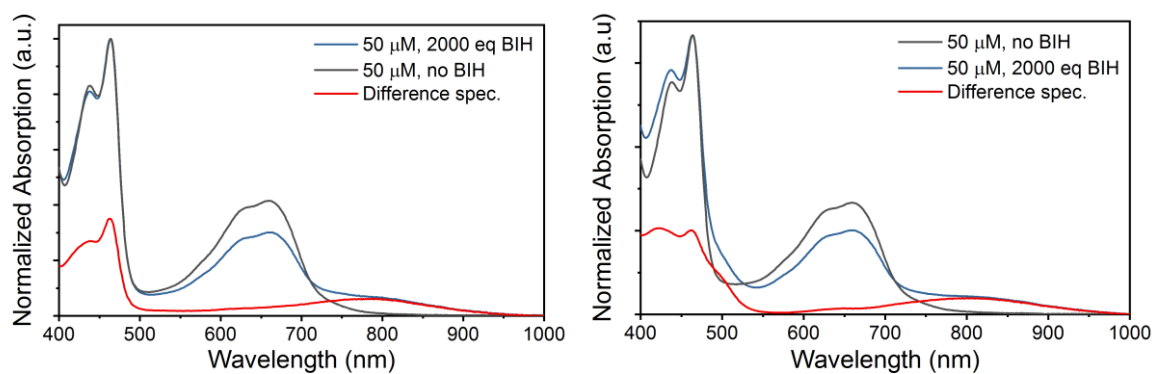


Figure S7: Normalized UV/Vis absorption spectra of **1** (left) and **2** (right) in MeCN (black) and in MeCN in the presence of 2000 equiv. (100 mM) BIH (blue). Deconvolution of the “blue” spectrum yields an additional species (Difference spec) with red-shifted absorption (red).

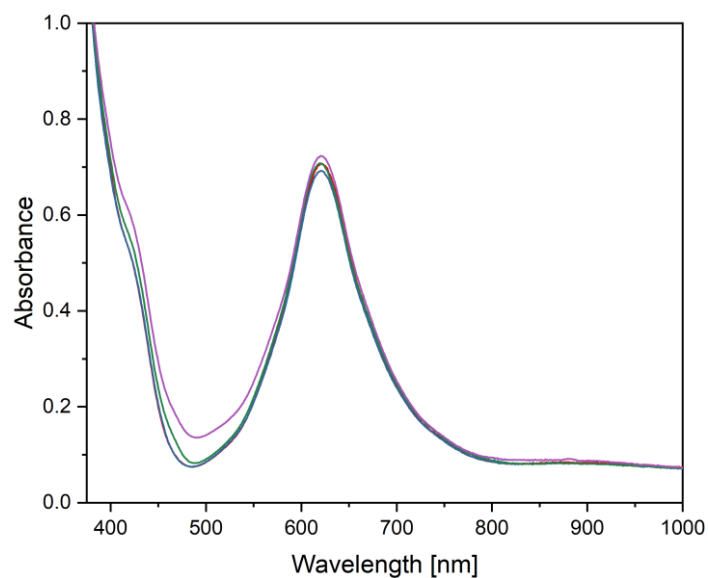


Figure S8: UV/Vis absorption spectra of **1<sup>red</sup>** formed in the photoreduction of **1** (50  $\mu$ M) in the presence of 25 mM (red), 50 mM (blue), 100 mM (green) BIH and 100 mM Et<sub>3</sub>N (purple), all in acetonitrile.

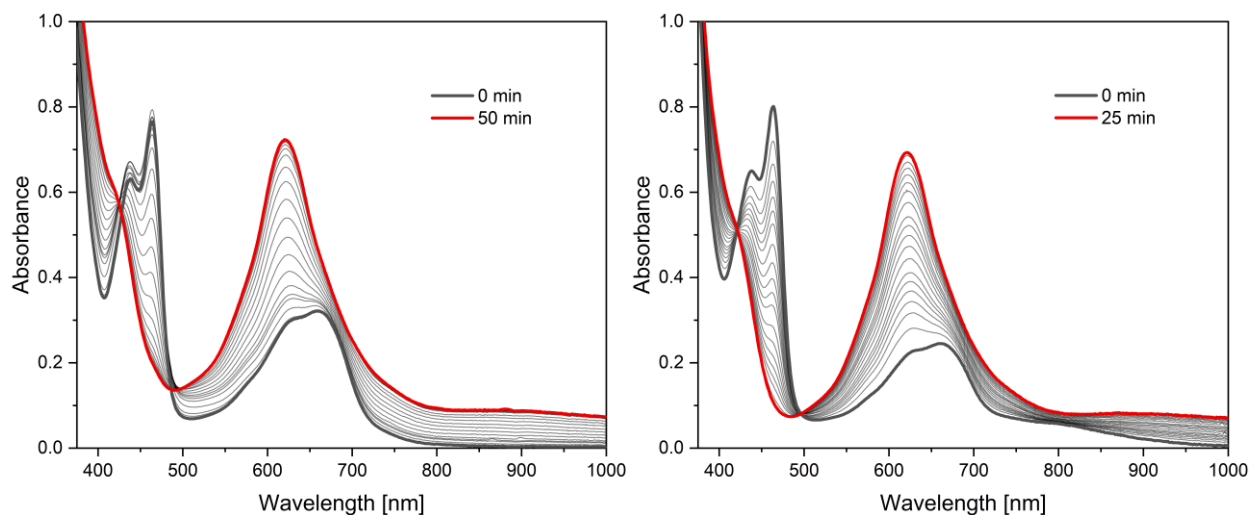


Figure S9: Spectral changes upon irradiation of **1** in MeCN in the presence of 2000 equiv. (100 mM) Et<sub>3</sub>N (left) and 2000 equiv. (100 mM) BIH (right).

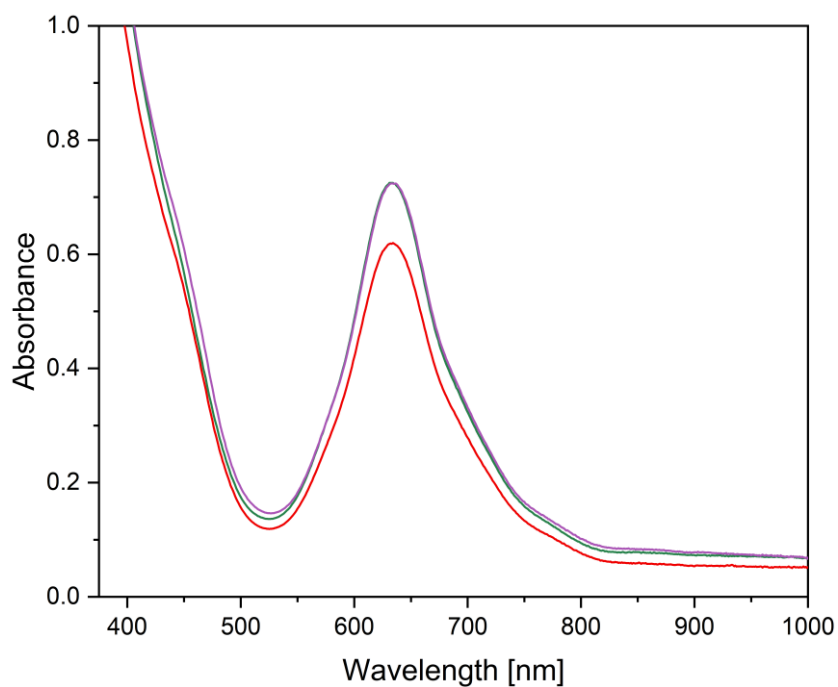


Figure S10: UV/Vis absorption spectra of **2<sup>red</sup>** formed in the photoreduction of **2** (50 μM) in the presence of 25 mM (red), 100 mM (green) BIH and 100 mM Et<sub>3</sub>N (purple), all in acetonitrile.

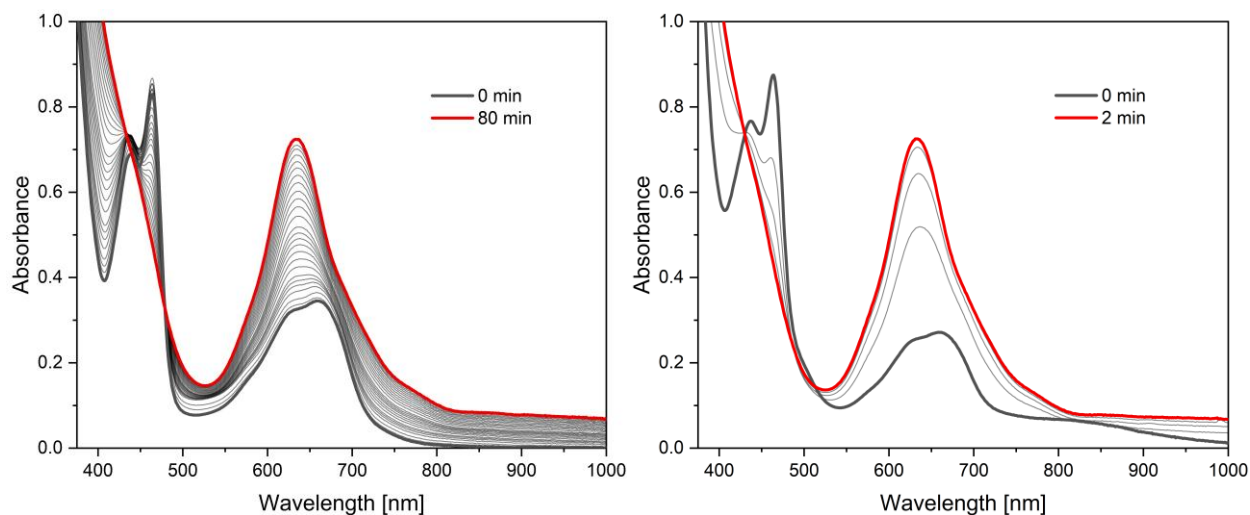


Figure S11: Spectral changes upon irradiation of **2** in MeCN in the presence of 2000 equiv. (100 mM) Et<sub>3</sub>N (left) and 2000 equiv. (100 mM) BIH (right).

Table S4: Quantum yields in the photoreduction of **1** to **1<sup>red</sup>** and **2** to **2<sup>red</sup>** in MeCN with different SEDs.

Reaction	100 mM Et <sub>3</sub> N	25 mM BIH	100 mM BIH
<b>1</b> to <b>1<sup>red</sup></b>	$3.3 \times 10^{-5}$	$3.2 \times 10^{-5}$	$1.1 \times 10^{-4}$
<b>2</b> to <b>2<sup>red</sup></b>	$1.6 \times 10^{-5}$	$8.9 \times 10^{-5}$	$9.7 \times 10^{-4}$

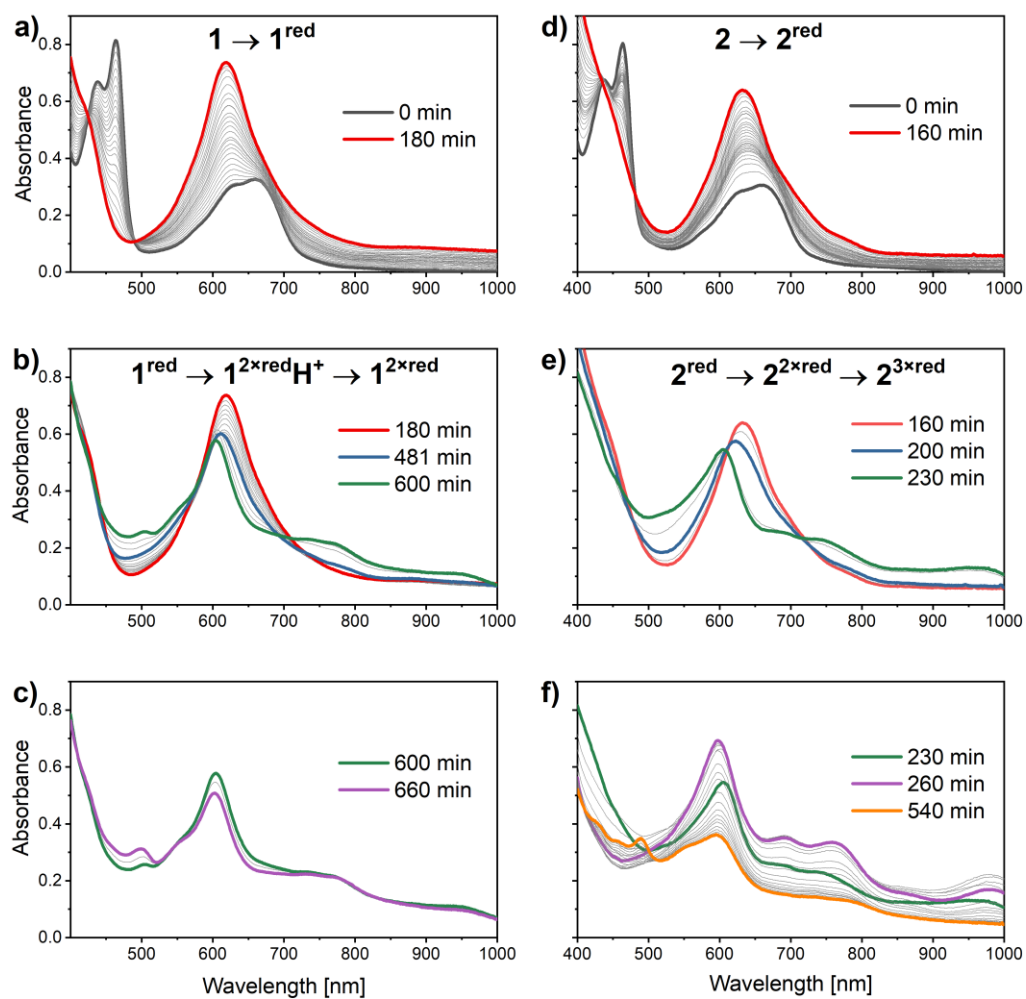


Figure S12: Spectral changes upon irradiation of **1** and **2** in MeCN in the presence of 500 equiv. (25 mM) BIH, showing the progression of a)  $\mathbf{1} \rightarrow \mathbf{1}^{\text{red}}$ ; b)  $\mathbf{1}^{\text{red}} \rightarrow \mathbf{1}^{2 \times \text{red}} \text{H}^+ \rightarrow \mathbf{1}^{2 \times \text{red}}$ ; d)  $\mathbf{2} \rightarrow \mathbf{2}^{\text{red}}$ ; e)  $\mathbf{2}^{\text{red}} \rightarrow \mathbf{2}^{2 \times \text{red}} \rightarrow \mathbf{2}^{3 \times \text{red}}$  c) & f) depict reaction pathways that we cannot assign and end in decomposition of the complexes.

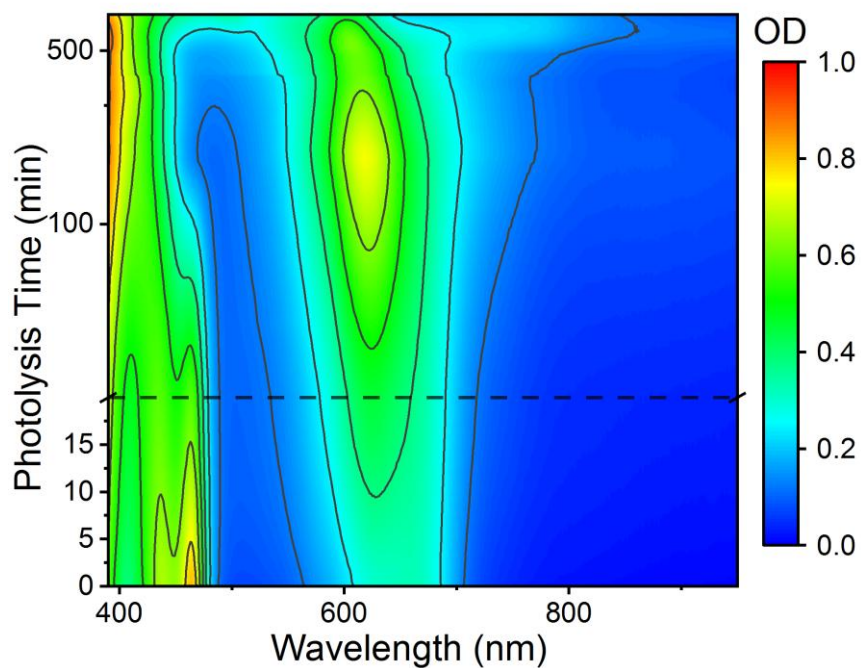


Figure S13: The absorption spectra of **1** during the complete photoreduction in MeCN in the presence of 500 equiv. BIH. Data shown in a two-dimensional Wavelength vs Time representation.

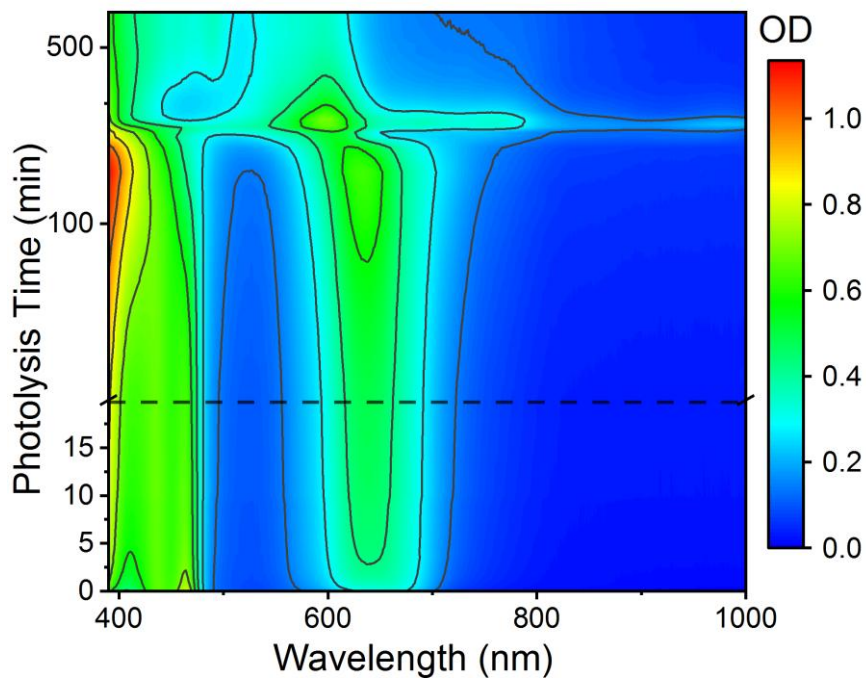


Figure S14: The absorption spectra of **2** during the complete photoreduction in MeCN in the presence of 500 equiv. BIH. Data shown in a two-dimensional Wavelength vs Time representation.

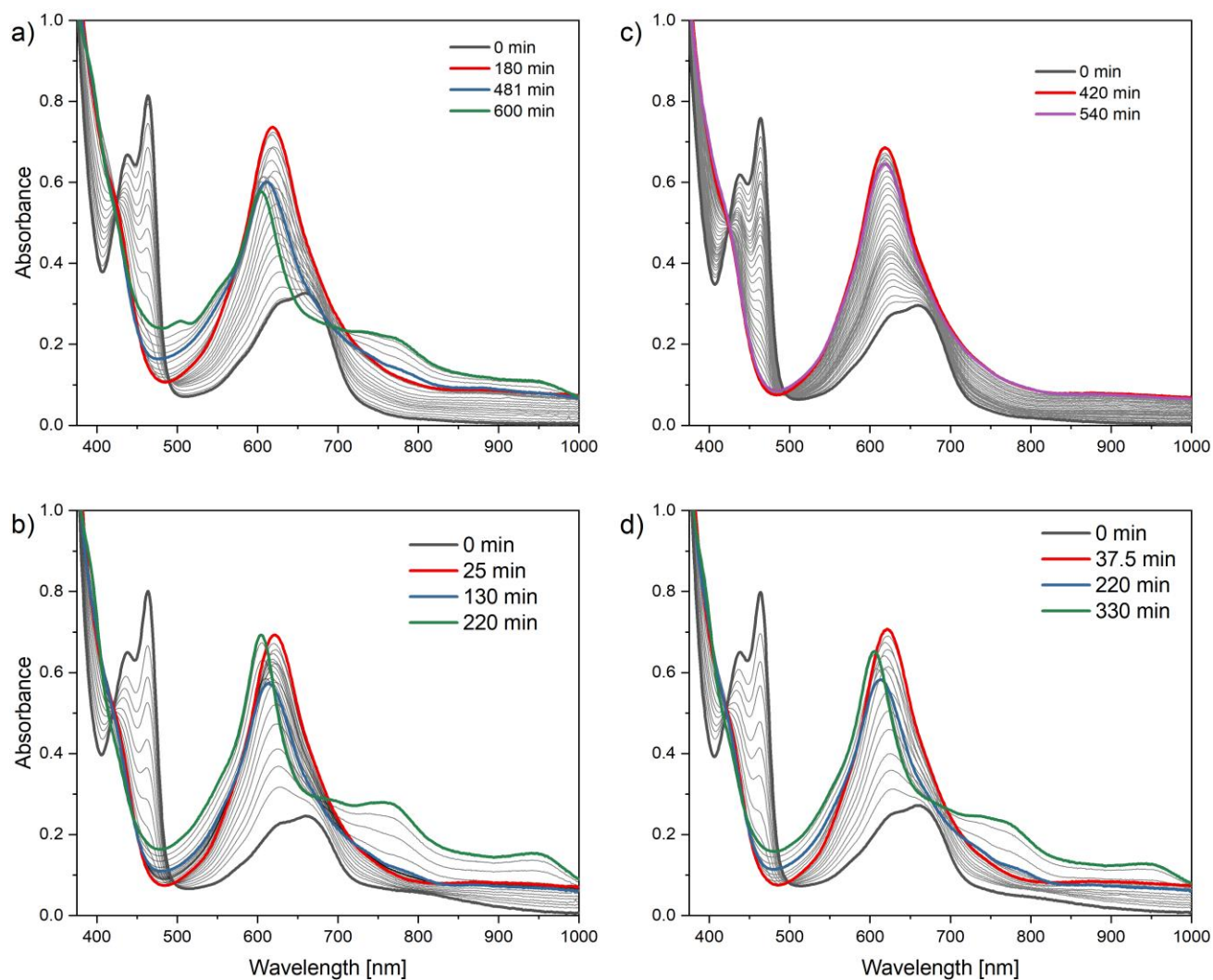


Figure S15: UV/Vis absorption spectra recorded during the photoreduction of **1** (50  $\mu$ M) in the presence of 25 mM (top) and 100 mM BIH (bottom) as a sacrificial reductant. The columns represent different batches of **1** which differ in reaction rates.

We noticed that different batches of **1** differ in terms of reaction times in the photoreduction experiments with BIH. The difference is more significant with 500 equiv. of BIH added, where the reduction of **1** to **1<sup>red</sup>** varies between 180 min and 420 min (Figure S15a&c). Due to the long irradiation times needed in the slow experiment, the clean formation of **1<sup>2 $\times$ red</sup>H<sup>+</sup>** and **1<sup>2 $\times$ red</sup>** could not be observed. The difference is less significant with 2000 equiv. BIH (Figure S15b&d). Independent of the batch, the reaction proceeds *via* the same species, i.e. **1<sup>red</sup>**, **1<sup>2 $\times$ red</sup>H<sup>+</sup>** and **1<sup>2 $\times$ red</sup>**, only the rate of the respective conversions differs.

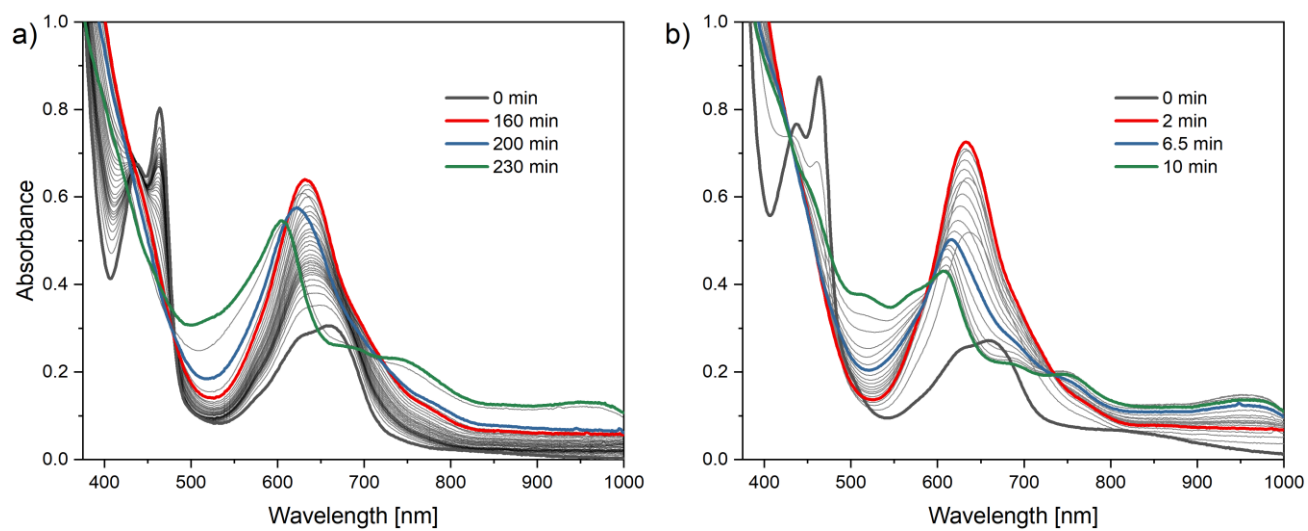


Figure S16: UV/Vis absorption spectra recorded during the photoreduction of **2** (50 μM) in the presence of 25 mM (left) and 100 mM BIH (right) as a sacrificial reductant.

## 8 Comparison of spectra: Photoreduction vs Electrolysis

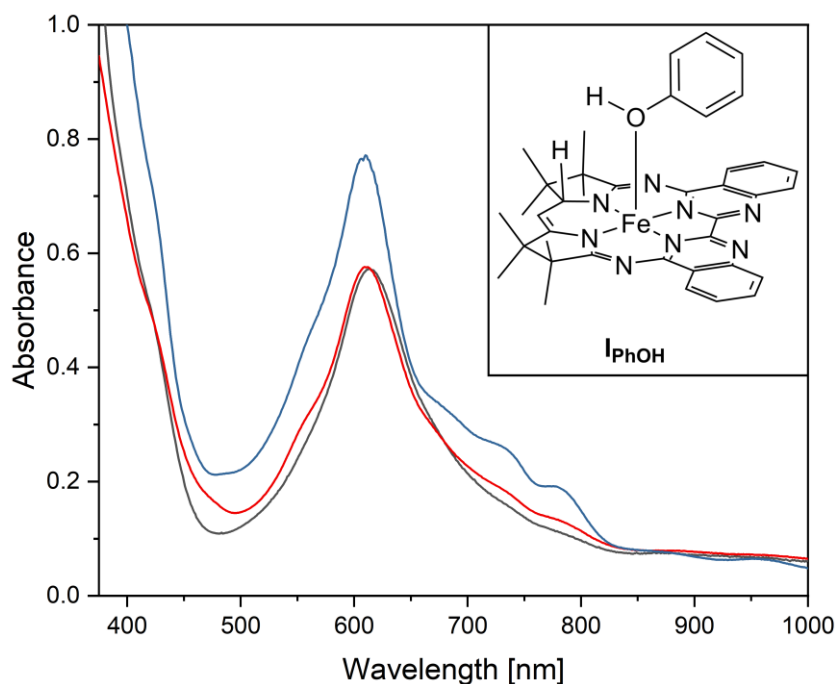


Figure S17: UV/Vis absorption spectrum in the photoreduction of **1** (50  $\mu\text{M}$ ) in MeCN at 100 mM BIH after 130 min (black) and the spectra of  $\mathbf{1}^{2\times\text{red}}\mathbf{H}^+$  in MeCN (red) and THF (blue).  $\mathbf{1}^{2\times\text{red}}\mathbf{H}^+$  in MeCN was obtained after bulk electrolysis of **1** at  $-2.10\text{ V}_{\text{Fc}}$  (see figure S18 for CV) and subsequent addition of 85 equiv. PhOH. The spectrum in THF was obtained by dissolving isolated  $\mathbf{1}^{2\times\text{red}}$  and subsequent addition of 85 equiv. PhOH.<sup>20</sup> The spectra of  $\mathbf{1}^{2\times\text{red}}\mathbf{H}^+$  were recorded at 98  $\mu\text{M}$  (MeCN) and 130  $\mu\text{M}$  complex (THF) and the absorbance plot shown here is scaled to 50  $\mu\text{M}$  for comparison with the spectrum from photoreduction. Inset: Structure of  $\mathbf{I}_{\text{PhOH}}$ .

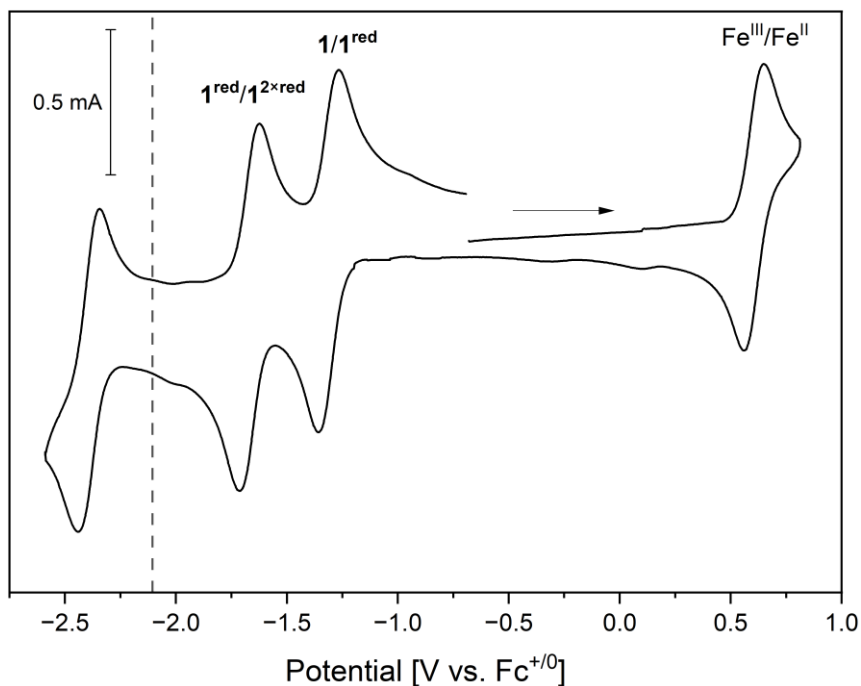


Figure S18: CV of a 0.5 mM solution of **1** in MeCN (0.1 M  $[N(n\text{-Bu})_4]PF_6$ , 100 mV/s scan rate). The dashed line represents the potential of the electrolysis to generate  $\mathbf{1}^{2\times\text{red}}$  ( $-2.10 V_{Fc}$ ).

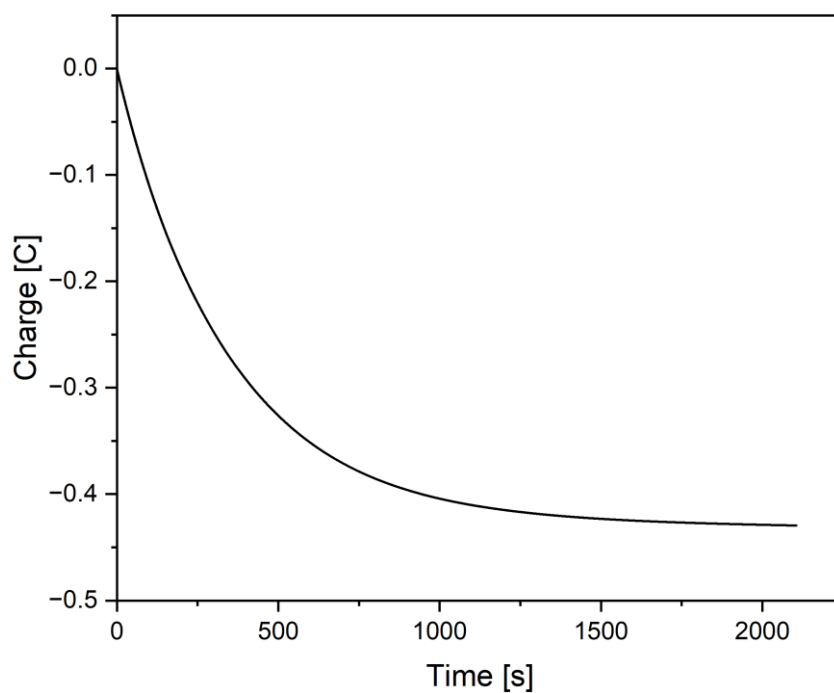


Figure S19: Charge over time plot for electrolysis of **1** at  $-2.10 V_{Fc}$  to generate  $\mathbf{1}^{2\times\text{red}}$ . In total,  $-0.65 C$  were passed, accounting for 2.28 equiv. of electrons.

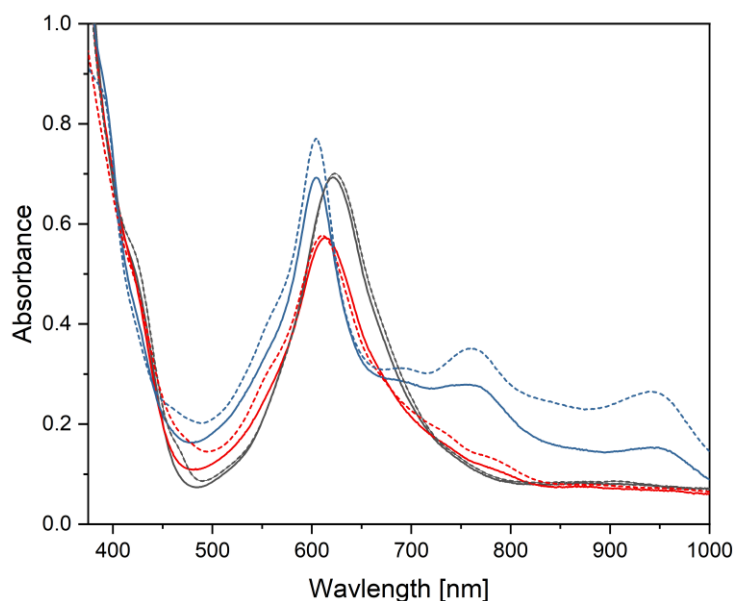


Figure S20: Solid: UV/Vis absorption spectra in the photoreduction of **1** (50  $\mu\text{M}$ ) in MeCN at 100 mM BIH after 25 min (black), 130 min (red) and 220 min (blue). Dashed: UV/Vis absorption spectrum of isolated **1<sup>red</sup>** in acetonitrile (black) and the spectra obtained after bulk electrolysis of **1** at  $-2.10\text{ V}_{\text{Fc}}$  before (blue) and after addition of 85 equiv. PhOH (red) to generate **1<sup>2 $\times$ red</sup>** and **1<sup>2 $\times$ red</sup>H<sup>+</sup>**. The spectra from bulk electrolysis were recorded at 98  $\mu\text{M}$  complex (MeCN) and the absorbance plot shown here is scaled to 50  $\mu\text{M}$  for comparison with the other spectra.

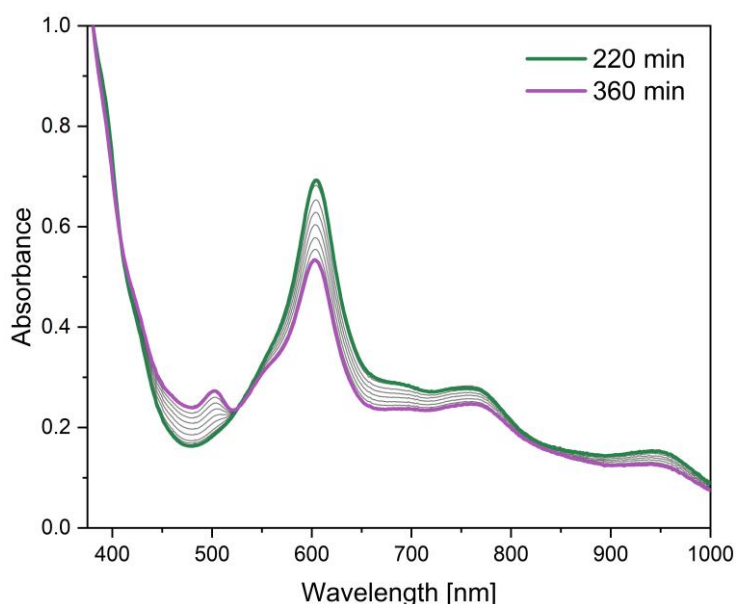


Figure S21: UV/Vis absorption spectra obtained subsequent to the formation of **1<sup>2 $\times$ red</sup>** upon irradiation of **1** (50  $\mu\text{M}$ ) in MeCN in the presence of 100 mM BIH as a sacrificial reductant.

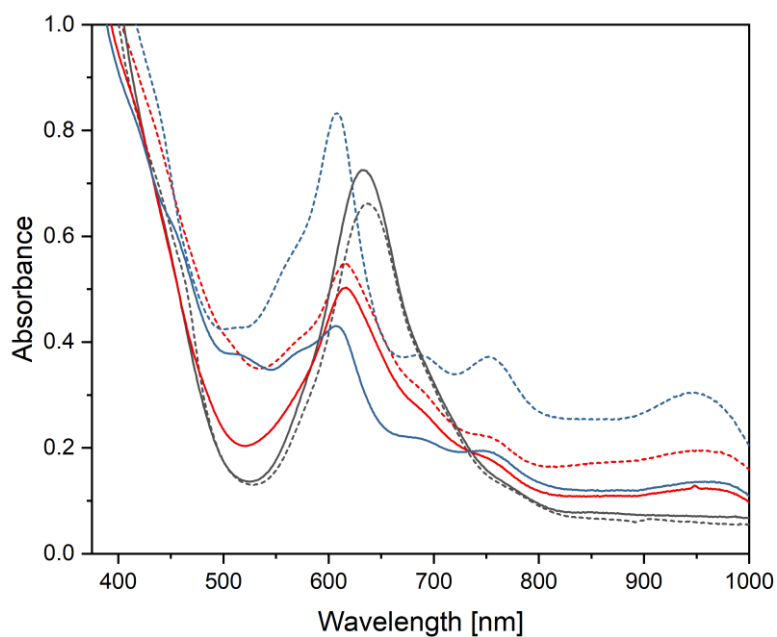


Figure S22: Solid: UV/Vis absorption spectra in the photoreduction of **2** in MeCN at 100 mM BIH after 2 min (black), 6.5 min (red) and 10 min (blue). Dashed: UV/Vis absorption spectrum of isolated **2<sup>red</sup>** in acetonitrile (black) and the spectra obtained after bulk electrolysis of **2** at  $-1.76 V_{Fc}$  (red) and  $-2.24 V_{Fc}$  (blue) to generate **2<sup>2×red</sup>** and **2<sup>3×red</sup>** (see figure S23 for CV). The concentration of complex in the samples from bulk electrolysis is 49  $\mu\text{M}$  (MeCN).

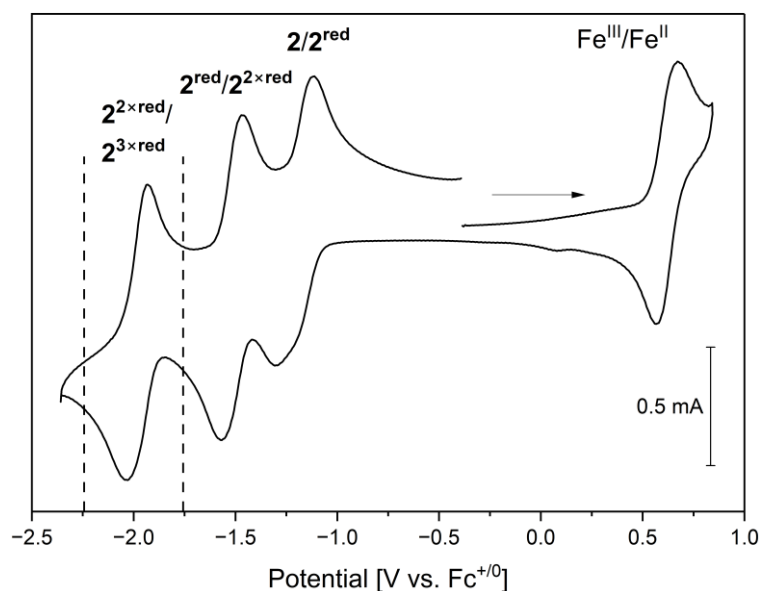


Figure S23: CV of a 0.5 mM solution of **2** in MeCN (0.1 M  $[\text{N}(n\text{-Bu})_4]\text{PF}_6$ , 100 mV/s scan rate). Dashed lines represent the potential of the electrolysis to generate **2<sup>2×red</sup>** ( $-1.76 V_{Fc}$ ) and **2<sup>3×red</sup>** ( $-2.24 V_{Fc}$ ).

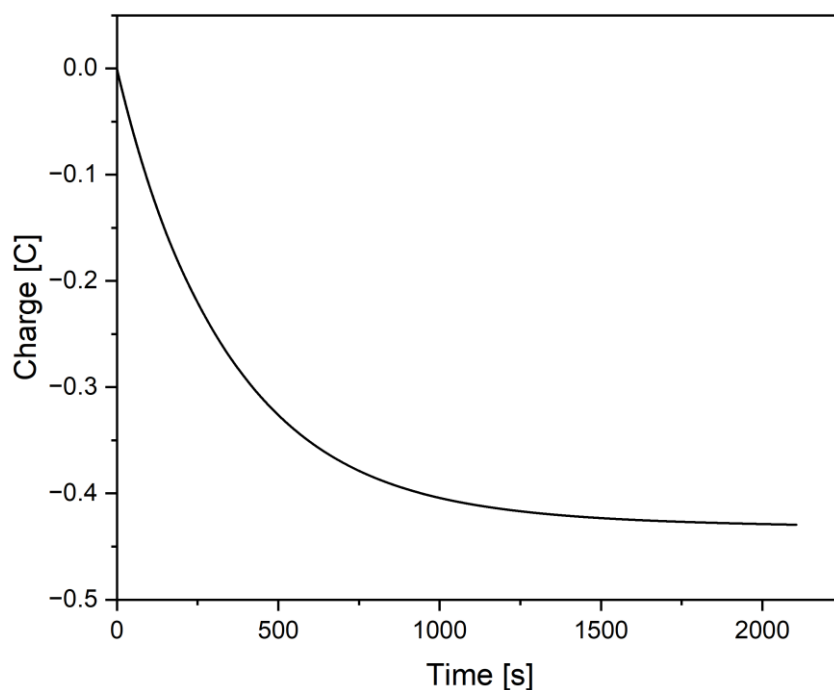


Figure S24: Charge over time plot for electrolysis of **2** at  $-1.76 V_{Fc}$  to generate  $\mathbf{2}^{2\times red}$ . In total,  $-0.43 C$  were passed, accounting for 2.23 equiv. of electrons.

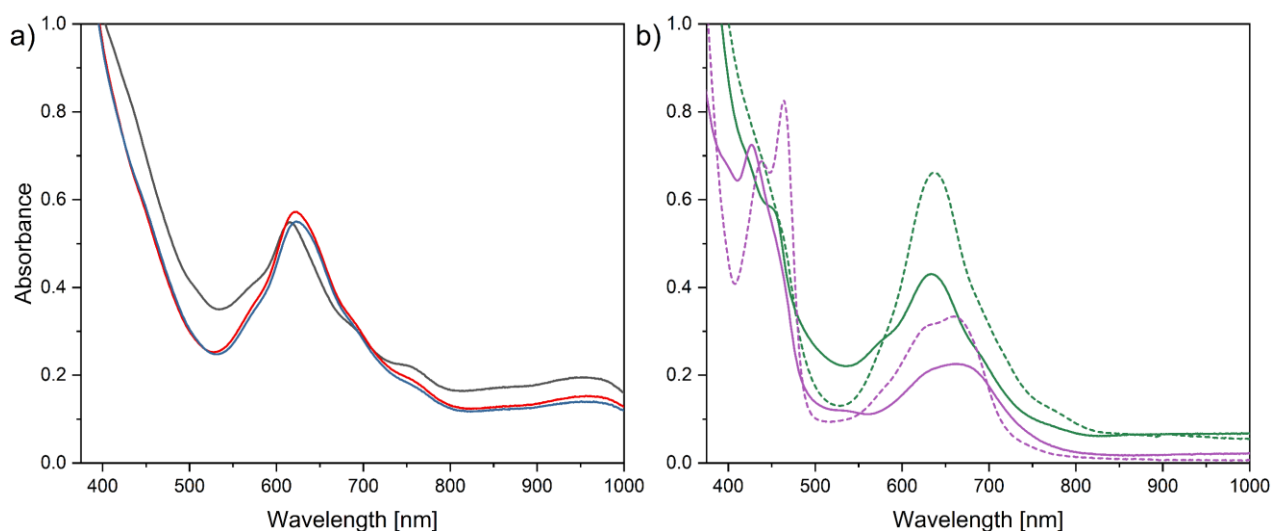


Figure S25: UV/Vis absorption spectra in MeCN obtained after bulk electrolysis of a solution of **2** at  $-1.76 V_{Fc}$  to generate  $\mathbf{2}^{2\times red}$  and after subsequent addition of 5 equiv. of different acids to the solution of the electrochemically reduced compound. Left:  $\mathbf{2}^{2\times red}$  (black), PhOH (red) and benzoic acid (blue). Right: triethylammonium chloride (green, solid) and *p*-toluenesulfonic acid (purple, solid). For comparison spectra of  $\mathbf{2}^{red}$  (green, dashed) and **2** (purple, dashed) are shown.

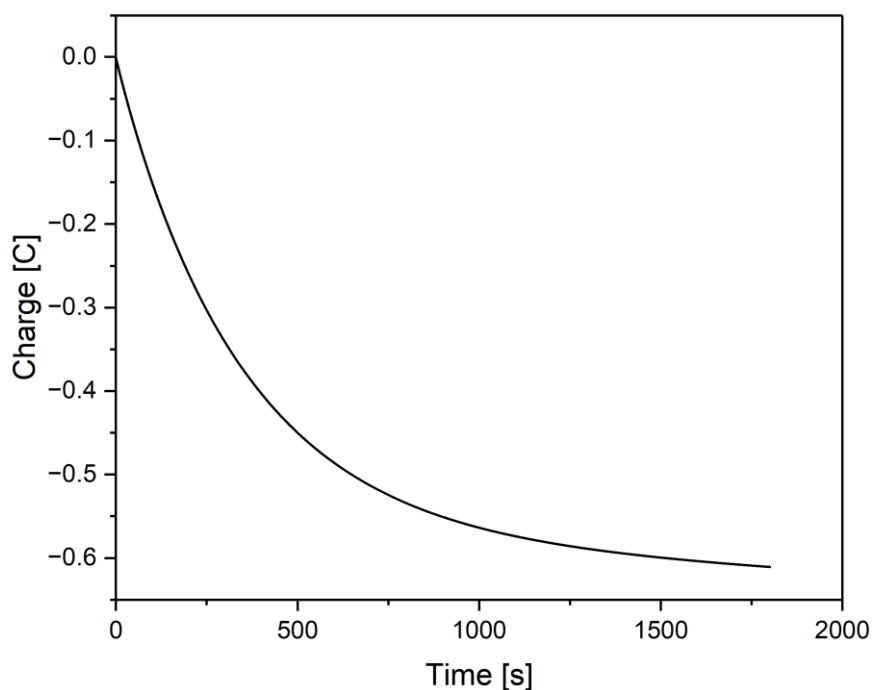


Figure S26: Charge over time plot for electrolysis of **2** at  $-2.24 V_{Fc}$  to generate  $\mathbf{2}^{3\times red}$ . In total,  $-0.61 C$  were passed, accounting for 3.16 equiv. of electrons.

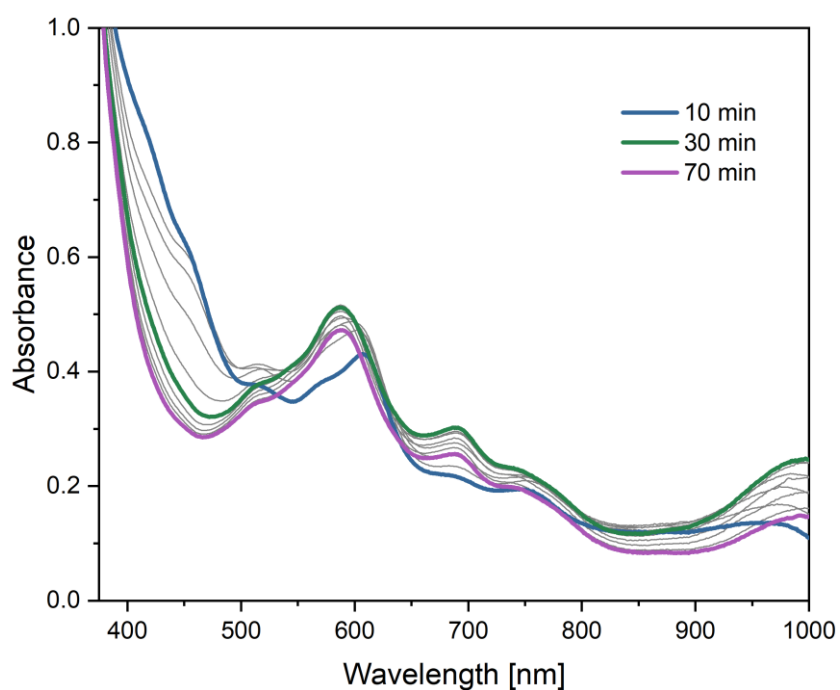


Figure S27: UV/Vis absorption spectra obtained subsequent to the formation of  $\mathbf{2}^{3\times red}$  upon irradiation of **2** ( $50 \mu M$ ) in MeCN in the presence of 100 mM BIH as a sacrificial reductant.

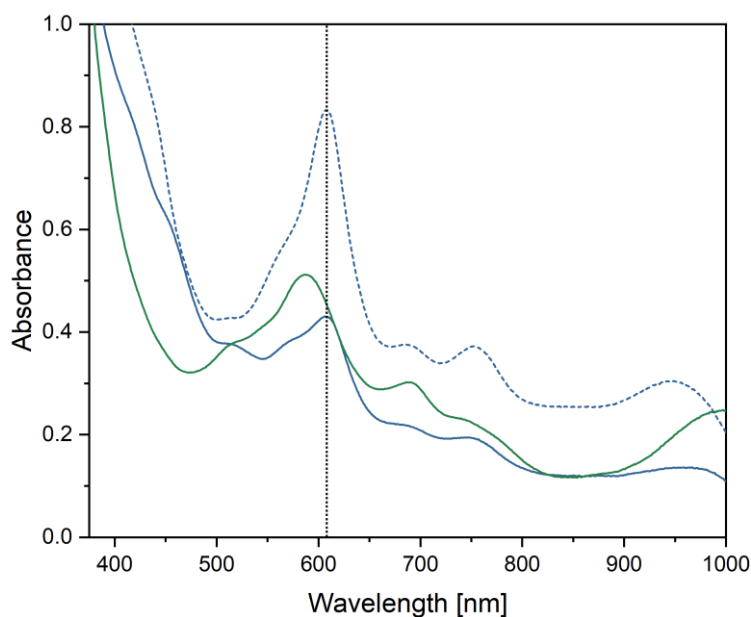


Figure S28: Comparison of the UV/Vis absorption spectrum obtained after 10 min (blue) and 30 min (green) irradiation of **2** (50  $\mu$ M) in MeCN in the presence of 100 mM BIH as a sacrificial reductant (solid) and of the spectrum obtained after bulk electrolysis of **2** at  $-2.24$  V<sub>Fe</sub> to generate **2**<sup>3×red</sup> (blue, dashed).

## 9 Photoreduction analysis

We form a more detailed picture of the photoreduction by separating the observed per-photon reduction quantum yield (QY) into individual contributions:

$$\Phi_{obs} = \Phi_{form} \cdot \Phi_{diff} \cdot \Phi_{red}$$

Here, the observed QY is separated into: 1) the yield of photochemical active states after excitation ( $\Phi_{form}$ ), 2) the yield of diffusion limited catalyst-reductant encounters ( $\Phi_{diff}$ ), and 3) the yield of successful reduction given a diffusional encounter ( $\Phi_{red}$ ). That is,  $\Phi_{red}$  is an aggregate of the yield of forward electron transfer on diffusional encounter and the cage escape yield.<sup>21</sup> Since the transient absorption data does not suggest branching of the excited state relaxation, we will assume a  $\Phi_{form} = 1$ , and all absorbed photons lead to an excited catalyst that can potentially be photoreduced.

The diffusion limited yield can be written in terms of the diffusion rate ( $k_d$ ), the reductant concentration ( $[BIH]$ ) and the excited-state lifetime of the catalyst in the absence of quencher ( $\tau$ )

$$\Phi_{diff} = \frac{k_d[BIH]}{\frac{1}{\tau} + k_d[BIH]}$$

Combining the observed yields and the diffusion limited yield, we can estimate the reduction yield per diffusional encounter. Any  $\Phi_{red}$  yield less-than or equal to 1 is consistent with simple diffusional/collisional reduction, while a yield of more than 1 will imply pre-association or other non-trivial kinetics, as a faster-than-diffusion reaction would be implied.

$$\Phi_{red} = \Phi_{obs} \cdot \frac{1}{\Phi_{form}} \cdot \left(1 + \frac{1}{\tau \cdot k_d[BIH]}\right) \approx \Phi_{obs} \cdot \left(1 + \frac{1}{\tau \cdot k_d[BIH]}\right)$$

Taking the catalyst excited-state lifetime as approximately 15 ps, the diffusion coefficient  $k_d$  as approximately  $10^9 \text{ M}^{-1}\text{s}^{-1}$  and the reductant concentration as 100 mM, the diffusion limited per-photon reduction is  $\sim 1.5 \cdot 10^{-3}$ . Our observed yields are well below this limit, and can thus be explained without *e.g.* pre-complexation.

As the excited-state lifetimes and diffusional rates of all compounds are similar, the higher observed per-photon reduction yields of **2** and **2<sup>red</sup>** compared to their monometallic counterparts implies a significantly larger probability of reduction per diffusional encounter.

<b>Reduction Step</b>	$\Phi_{obs}$ ( $\times 10^{-4}$ )	$\Phi_{red}$
<b>1</b> $\rightarrow$ <b>1<sup>red</sup></b>	1.1	0.073
<b>2</b> $\rightarrow$ <b>2<sup>red</sup></b>	9.7	0.65
<b>1<sup>red</sup></b> $\rightarrow$ <b>1<sup>2<math>\times</math>red</sup>H<sup>+</sup></b>	0.40	0.027
<b>2<sup>red</sup></b> $\rightarrow$ <b>2<sup>2<math>\times</math>red</sup></b>	0.90	0.060

## 10 $\text{Fe}^{\text{III}}(\text{Mabiq})\text{Cl}_2$ Photochemistry

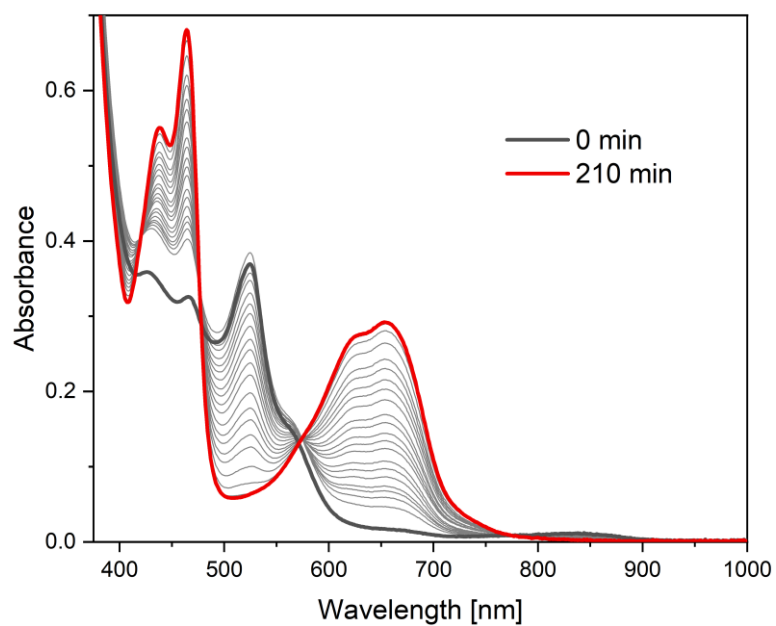


Figure S29: Spectral changes upon irradiation of  $\text{Fe}^{\text{III}}(\text{Mabiq})\text{Cl}_2$  ( $50 \mu\text{M}$ ) in a DCM/MeCN (1:1) mixture in the absence of a sacrificial reductant.

## References

1. B. D. McCarthy, D. J. Martin, E. S. Rountree, A. C. Ullman and J. L. Dempsey, *Inorganic Chemistry*, 2014, **53**, 8350-8361.
2. E. Mueller, G. Bernardinelli and A. Von Zelewsky, *Inorganic Chemistry*, 1988, **27**, 4645-4651.
3. P. Banerjee, A. Company, T. Weyhermüller, E. Bill and C. R. Hess, *Inorganic Chemistry*, 2009, **48**, 2944-2955.
4. K. Rickmeyer, M. Huber and C. R. Hess, *Chemical Communications*, 2024, **60**, 819-822.
5. L. Shaw, D. M. U. K. Somisara, R. C. How, N. J. Westwood, P. C. A. Bruijninx, B. M. Weckhuysen and P. C. J. Kamer, *Catalysis Science & Technology*, 2017, **7**, 619-626.
6. I.-S. H. Lee, E. H. Jeoung and M. M. Kreevoy, *Journal of the American Chemical Society*, 1997, **119**, 2722-2728.
7. N. Elgrishi, M. B. Chambers and M. Fontecave, *Chemical Science*, 2015, **6**, 2522-2531.
8. R. Lauenstein, S. L. Mader, H. Derondeau, O. Z. Esezobor, M. Block, A. J. Römer, C. Jandl, E. Riedle, V. R. I. Kaila, J. Hauer, E. Thyrhaug and C. R. Hess, *Chemical Science*, 2021, **12**, 7521-7532.
9. U. Megerle, R. Lechner, B. König and E. Riedle, *Photochemical & Photobiological Sciences*, 2010, **9**, 1400-1406.
10. M. Grübel, I. Bosque, P. J. Altmann, T. Bach and C. R. Hess, *Chemical Science*, 2018, **9**, 3313-3317.
11. H. S. Stark, P. J. Altmann, S. Sproules and C. R. Hess, *Inorganic Chemistry*, 2018, **57**, 6401-6409.
12. G. Sheldrick, *Bruker AXS Inc., Madison, Wisconsin, USA*, 2007.
13. CrysAlisPro, Scale3 Abspack, Rigaku Oxford Diffraction, 2019.
14. G. Sheldrick, *Acta Crystallographica Section A*, 2015, **71**, 3-8.
15. G. Sheldrick, *Acta Crystallographica Section C*, 2015, **71**, 3-8.
16. O. V. Dolomanov, L. J. Bourhis, R. J. Gildea, J. A. K. Howard and H. Puschmann, *Journal of Applied Crystallography*, 2009, **42**, 339-341.
17. G. Sheldrick, *Acta Crystallographica Section A*, 2008, **64**, 112-122.
18. C. F. Macrae, P. R. Edgington, P. McCabe, E. Pidcock, G. P. Shields, R. Taylor, M. Towler and J. van de Streek, *Journal of Applied Crystallography*, 2006, **39**, 453-457.
19. A. Kumar, P. Malevich, L. Mewes, S. Wu, J. P. Barham and J. Hauer, *The Journal of Chemical Physics*, 2023, **158**, 144201.
20. K. Rickmeyer, L. Niederegger, M. Keilwerth and C. R. Hess, *ACS Catalysis*, 2022, **12**, 3046-3057.
21. C. Wang, H. Li, T. H. Bürgin and O. S. Wenger, *Nature Chemistry*, 2024, **16**, 1151-1159.